Modelling study of wave damping over a sandy and a silty bed

Linlong Tong[1,2], Jisheng Zhang[1,2,*], Jialin Zhao[2], Jinhai Zheng[1,2,*], Yakun Guo[3]

1 Key Laboratory of Coastal Disaster and Defence (Hohai University), Ministry of Education, Nanjing, China

2 College of Harbor, Coastal and Offshore Engineering, Hohai University, Nanjing, China

3 Faculty of Engineering and Informatics, University of Bradford, Bradford, BD7 1DP, UK

* Corresponding author: jszhang@hhu.edu.cn; jhzheng@hhu.edu.cn

Abstract

Laboratory experiments have been carried out to investigate wave damping over the seabed, in which the excess pore pressure and free surface elevations are synchronously measured for examining the wave-induced soil dynamics and wave kinematics. Two types of soil, namely fine sand and silt, are tested to examine the role of soil in the wave damping. Observation of experiments shows that (i) soil liquefaction takes place for some tests with silty bed and soil particles suspend into the water layer when the bed is made of silt; (ii) sand ripples can be generated for experiments with sand bed. Measurements reveal that the wave damping greatly depends on the soil dynamic responses to wave loading and the wave damping mechanism over the silty seabed differs from that over the sand bed. On the one hand, the wave damping rate is greatly increased, when soil liquefaction occurs in the silty bed. On the other hand, the presence of sand ripples generated by oscillatory flow in the sand bed experiments also increases the wave damping to some extent. Furthermore, experimental results show that soil particle suspension in the silt bed test contributes to the wave damping. Theoretical analysis is presented to enhance discussions on the wave damping. The theoretical calculations demonstrate that the wave damping is mainly induced by the shear stress in the boundary layer for the cases when no liquefaction occurs. While for the cases when soil liquefaction takes place, the viscous flow in the liquefied layer contributes most towards to the wave damping.

Keywords： Wave damping rate; Bottom boundary layer; Viscous flow; Liquefaction; Sand ripple.

1. Introduction

In shallow water, the interaction of waves with the seabed results in a number of phenomena, such as shoaling, refraction and diffraction. Such wave-seabed interaction also leads to wave energy dissipation as reported by Gade (1958), Hisao and Shemdin (1980), Elgar and Raubenheimer (2008), Traykovski et al. (2014), Hsu et al. (2018) and Zhu et al. (2019). For a rigid or almost rigid seabed, wave energy can be dissipated due to the shear flow in a laminar or turbulent boundary layer. For the seabed which is composed of coarse sand or shingle, it can be treated as a porous medium with good permeability. The seepage flow occurring in such seabed can generate wave energy dissipation. For a non-rigid or flexible seabed, energy dissipation becomes more complex and associates with the seabed sediment rheology. Since coastal sediments have a wide range of rheological properties, it is difficult to describe them with a single constitutive law (Liu et al., 2007). Despite the complexity of wave damping in shallow water, it is very important to understand its mechanism. On the one hand, the wave damping reduces the tendency of wave breaking, which has great influence on the sediment transportation (Zhang et al., 2017). On the other hand, the wave damping should be considered in the design of the coastal and offshore engineering.

Due to its practical engineering importance and application, the wave damping mechanism has been widely studied in the past decades. Under the small amplitude and linear wave assumptions, Putnam and Johnson (1949) studied the wave energy dissipation in the turbulent boundary layer. A friction coefficient, instead of the eddy viscosity coefficient, was introduced and a formula for the bottom friction dissipation was derived to describe the tangential stress at the seabed bottom and the wave damping, respectively. Although their study established a framework for studying the viscous damping in the turbulent boundary layer, the proposed formulation was not sufficiently rigorous as the expression of the friction coefficient was not clear. Following this work, a number of studies (for example, see Jonsson, 1966; Kampluis,

1978; Le Roux, 2012; Nielsen, 1992; Zhang et al., 2014) have been carried out to determine the friction coefficient for viscous damping in the turbulent boundary layer. For the boundary layer of long wave, Liu and Orfila (2004) studied the viscous damping by using a perturbation approach and the Boussinesq approximation. A new set of Boussinesq equations for transient long-wave propagation were derived by considering the viscous effect, and their theoretical results agreed well with the experimental results of Liu et al. (2006).

For the percolation damping, Putnam (1949) developed a theory for the linear wave damping over a permeable seabed by ignoring the change of the pressure variation at the water-seabed interface. As such, his theory showed that the wave height did not decrease along downstream direction as firstly pointed out by Reid and Kajiura (1957). To overcome this drawback, Reid and Kajiura (1957) simultaneously solved the flow in the water domain and the seepage flow in the seabed. They presented the linear solutions for the wave motion and modified the linear wave dispersion relation with consideration of the percolation damping. However, their linear solutions become inappropriate in the nearshore region where the wave amplitude can no longer be considered negligible comparing with the water depth. To improve the simulation in the nearshore region, Packwood and Peregrine (1980) investigated the effect of the nonlinearity on the wave amplitude damping of long wave, such as solitary waves and bores. Liu et al. (2007) further studied the percolation damping of long wave over an unsaturated seabed. Their study indicated that momentary liquefaction might take place in an unsaturated seabed due to the seepage flow.

The above studies all considered the seabed as a rigid material, which is not accurate for the deformable seabed. In fact, considerable seabed deformation (e.g. seabed liquefaction) may be generated due to wave and seabed interaction. For such a non-rigid seabed, the primary problem is how to describe the strain-stress relationship. To this end, a number of constitutive models have been developed. Dalrymple and Liu

(1978) treated both the soft mud bed layer and overlaying water layer as viscous fluid and developed a two-layer viscous fluid model to study the wave motion over a mud bed. Their theory agreed well with the experimental data obtained by Gade (1958). However, the solutions of Dalrymple and Liu (1978) are implicit and in the core region of water layer, water viscosity can be ignored as the velocity gradient there is very small. This means that the analysis can be simplified. For example, Ng (2000) established a two-layer Stokes' boundary layer model to investigate the flow kinematics in a mud bed. Furthermore, measurements indicate that water viscosity is in the order of 10^{-6} m^2/s and is much smaller than that of the mud seabed (Gade, 1958; Wen and Liu, 1998), which can be in the order of 1 m^2/s. Therefore, the thickness of the boundary layer for the water column is much smaller than that for the viscous mud, attributing to higher order effects. Liu and Chan (2007, hereafter referred as LC) only mainly considered the viscosity of mud bed in calculating the damping rates resulted from the interaction of long progressive waves and solitary waves with mud beds. LC's theory and solutions are well confirmed by the recent experiments conducted by Park et al. (2008). In addition, visco-elastic model (Garnier et al., 2013; Macpherson, 1980; Mei et al., 2010) and Bingham-plastic model (Chan and Liu, 2009; Mei and Liu, 1987) were also developed to investigate the wave damping due to the interaction with seabed.

Most aforementioned studies focused on investigating the wave kinematics and the wave amplitude damping over a porous seabed without considering the seabed dynamic responses (e.g. the soil liquefaction and the bed deformation due to sediment transport) to wave loading (Foda and Tzang, 1994; Sumer et al., 2006; Kirca et al., 2013). The seabed liquefactions, including momentary liquefaction and residual liquefaction, have been observed in the field (Sassa, 2006) and wave flumes (Kirca et al., 2013; Tong et al., 2018). Such soil liquefaction may cause the failure of the offshore engineering structures. As such, extensive studies have been carried out to investigate the soil dynamics and liquefaction instability in the seabed and around the

marine structures (Zhang, et al., 2011; Zhang, et al., 2012; Sui et al. 2016, 2017; Lin, et al., 2016, 2017; Zhao, et al., 2017; Sun et al. 2019). However, little attention was paid to the wave damping induced by seabed liquefaction. In this study, laboratory experiments are carried out to examine the wave damping over a sandy bed and a silty bed. Pore pressure and wave height are synchronously measured during the experiments to evaluate the seabed response and the wave damping. The primary wave damping mechanism for waves interacting with two types of seabed has been discussed by using analytical approach.

2. **Experiments**

This study mainly focuses on progressive waves damping over the sandy and silty beds. Experimental set-up, experimental procedure and experimental conditions are described below.

2.1. Experimental set-up

Experiments are carried out in a wave flume with a dimension of 48 m (length) × 0.5 m (width) × 1 m (height) in Hohai University. Two sloping beaches are installed at two ends of the flume to absorb the wave energy in order to reduce the effect of the reflection on experiments. A hydraulic piston-type wave maker is installed upstream close to the beach by which linear waves, Stokes waves, solitary waves and random waves with wave height up to 20 cm and wave period between 0.6 s and 2.5 s can be generated. A sediment basin of 0.4 m high and 0.5 m wide is placed at the middle of the flume. For the sandy bed tests, the basin length is 3 m, while it is 5.3 m for the silty bed tests. In the experiments, four miniature pore pressure transducers (PPTs), whose diameter is 6 mm and covered by an argil filter, are utilized to measure the excess pore pressure within the seabed. The accuracy of these PPTs is 0.5%. The free water surface displacement is synchronously measured using capacitive wave gauges whose measurement accuracy is 0.5%. The arrangement of the PPTs and the wave

gauges are shown in Figure 1.

Experimental soil is the commercially available silica flour, which mainly consists of mineral composition of silica and alumina. Both the sand and silt are filter-type soils with the mean grain size of 0.147 mm and 0.042 mm, respectively. Physical properties of the soils are listed in Table 1, in which the relative density is defined by

$$D_r = \frac{e_{\max} - e}{e_{\max} - e_{\min}} \tag{1}$$

where $e_{\max}$ and $e_{\min}$ are the maximum and minimum void ratio of the grain, respectively. Since the soil particles are well-sorted, the clay content is small. The geometric standard deviation of particle size is 1.44 for the sand and 1.91 for the silt. The sample is taken from the point 20 cm below the mud-line in the middle of the basin after the experiment.

2.2. Experimental procedure

Before depositing test soils, the sediment basin is filled with water and PPTs are installed at the pre-designated locations under water for de-airing considerations. For fully saturated conditions, the sand bed is carefully prepared by means of sandy raining technique (Qi and Gao, 2014), as the settling velocity of the sand particles is large enough and the viscosity of the sand is very small. However, this technique is not applicable to the silt bed. This is because the silt particle is too fine with large viscosity and settles very slowly. During the settling, some particles adhere together to form large flocs. Therefore, the silt is first mixed with water in a container to form slurry which is slowly injected into the sediment basin. The processes of mixing and deposition of the test soil is repeated until the slurry fills the whole basin. Then the flume is slowly filled with clean water to a constant depth of 35 cm. Test soil is then left in the basin to consolidate for three days. The prescribed incident wave is generated by the hydraulic piston-type wave maker. A multichannel synchronous acquisition system is used to collect the wave height and pore pressure measurements

177 by using the wave gauges and PPTs. The sampling frequency is set to be 50 Hz for the
178 wave gauges and 33 Hz for the PPTs.
179
180 2.3. Experimental conditions
181 To evaluate the wave damping effectively, water depth, h' (hereafter prime indicates
182 that the variable is dimensional), is selected relatively shallow with a constant of 30
183 cm for the sandy bed tests. For the silty bed tests, water depth is increased to 35 cm to
184 avoid the large mass silt transportation. Observation shows that the steady state for the
185 sandy bed tests reaches after 10 minutes of the wave loading. While for the silty bed
186 tests, the wave loading is continuous until the pore pressure reaches approximately the
187 maximum value. Other detail test conditions are summarized in Table 2, in which H_0'
188 is the incident wave height; ω' is the wave frequency; u_{bm}' is the amplitude of free
189 stream velocity. which can be calculated as (Jonsson, 1966):

190 $$u_{bm}' = \frac{\omega' H_0'}{2\sinh k'h'} \tag{2}$$

191 where k' is the wave number. *Re* in Table 2 is the wave Reynolds number and given by

192 $$Re = \frac{u_{bm}' a_m}{\nu_m}, \qquad a_m = \frac{u_{bm}'}{\omega'} = \frac{H_0'}{2\sinh k'h'} \tag{3}$$

193 where ν_m is the viscosity of the liquefied layer. In Table 2, δ_w' and δ_m' are the
194 thickness of the Stokes boundary layer for water and liquefied soil, namely
195 $\delta_w' = \sqrt{2\nu_w/\omega'}$ and $\delta_m' = \sqrt{2\nu_m/\omega'}$; λ is the characteristic wave steepness defined by

196 $$\lambda = \frac{\omega'^2 H_0'}{2g} = 1 \tag{4}$$

197 where g is the acceleration of gravity. As suggested by Wen and Liu (1998), the
198 kinematic viscosity of sand and water mixture is negligible so that δ_m' for the sandy
199 bed is ignored. However, for the silty bed, the viscosity of the liquefied layer, ν_m, is as
200 large as 0.11 m^2/s, which is over 10^5 times larger than that of pure water, ν_w.

3. Results and discussions

Sand and silt have different grain sizes and mechanic properties, which result in their different responses to wave loading. Such different responses in turn affect differently the wave motion and the associated wave damping, as described below.

3.1. Wave-induced pore pressure in seabed

It is observed that the pore pressure response of the wave-seabed interaction is clearly different between the sandy bed tests and the silty bed tests. In the sandy bed tests, the pore pressure oscillates with time and the period-averaged pore pressure, namely the residual pore pressure, is almost zero. This result, which is consistent with the former studies (Chang et al., 2007; Yamamoto et al., 1978), is because that the sand bed has relatively larger permeability which is in the order of magnitude of $O(10^{-3}$ m/s)~$O(10^{-6}$ m/s) and strong rigidity. Soil deformation is very small and as such pore water can drain out quickly. During this process, the amplitude and phase lag of pore pressure in vertical profile are very important to the stability of the seabed. Figure 2 shows the distribution of the amplitude of excess pore pressure $p_{0\max}$, which is normalized by the amplitude of the dynamic water pressure at the interface p_b'. In Figure 2, lines represent the analytical solutions proposed by Hsu and Jeng (1994) for wave-induced pore pressure in finite thickness seabed; D' is the thickness of the seabed, G is the soil shear modulus, K_w is the bulk modulus of elasticity of pure water, v is the Poisson's ratio, and S_r is the saturation degree of the sandy seabed. In general, the agreement between the experimental data and analytical results is good. The phase lag of oscillatory pore pressure is also observed in the sandy bed tests because of the permeability and hydraulic gradient effects (Okusa, 1985). On the other hand, the sandy bed is highly saturated so that the observed phase lags are smaller than 38°.

The direct observation of the experiments for wave propagating over sand bed

shows that there is no soil liquefaction taking place. Using the measured pore pressure and according to the liquefaction criteria proposed by Zen and Yamazaki (1991), such soil liquefaction criteria is not met for all sandy bed tests, which confirms the direct observation in this study.

However, in the silty bed tests, wave-induced pore pressure within the seabed p'_m consists of two parts, namely the residual pore pressure $\overline{p}$ and the oscillatory pore pressure $\tilde{p}$. Figure 3 is an example of the time series of the excess pore pressure for tests No. 6, 7 and 8. It can be seen that $\overline{p}$ is significant and much larger than the oscillatory pore pressure at depth of 9 cm and 27 cm in test No 7 and 8 (see Figure 3(*e*, *f*, *h*, *i*)). It is well known that the pore pressure accumulation within the seabed is mainly ascribed to the fact that the pore water cannot drain out during the wave cycle due to the large plastic deformation and weak permeability of the bed medium. As suggested by Seed and Rahman (1978), the soil will be liquefied when the residual pore pressure ($\overline{p}$) exceeds its initial vertical effective stress σ'_{v0} , namely

$$\overline{p} \geq \sigma'_{v0} = -\gamma'\left(z' + h'\right) \tag{5}$$

in which the vertical coordinate axis starts from the free surface with positive upward and the horizontal coordinate axis starts from the left side of the sediment basin with positive rightward. Based on the above criteria, soil liquefaction occurs for all silty bed tests except test No. 6. In Figure 3, the onset of liquefaction for each test is marked by red arrow. Analysis of the detailed measurements indicates that the liquefaction depth, *d′*, is in the range of 2 cm to 9 cm for test No. 7, 9 cm to 27 cm for test No. 8 and 27 cm to 40 cm for test No. 9.

3.2. Wave damping in non-liquefaction tests

For non-liquefaction tests, the displacement of the water-seabed interface is negligible. Wave energy dissipation over a non-liquefaction seabed is usually owing to the shear stress in the laminar or turbulent boundary layer or the seepage flows within the

seabed. In the experiments, sand ripples are observed to be formed in the test No. 3 and test No. 5, as it is shown in Figure 4. The measured free surface elevations indicate that the wave height damping is less than 1% in test No. 1, 2 and 4 where no sand ripples are formed. When sand ripples are formed, the wave damping increases to 3.6% in test No. 3, 4.1% in test No. 5 and 5.6% in test No. 6, as shown in Figure 5. To investigate the wave damping in more details, two main damping mechanisms causing the wave damping, namely the percolation damping and viscous damping mechanism, are examined and discussed, respectively.

For the percolation damping, Packwood and Peregrine (1980) proposed that the energy dissipation rate, d_p, could be calculated by integrating the rate of working done by pressure at the bottom boundary over the wave length:

$$d_p = \int_{x_0}^{x_0+L} p'_m \frac{k_s}{\rho g} \frac{\partial p'_m}{\partial z'}\bigg|_{z'=-h'} dx' \tag{6}$$

where x_0 is the start location, L is the wavelength and ρ is the density of water. Normalizing the pressure (p'_m) and displacement (x', z') by $\rho g H'/2$ and L, D', respectively, yields:

$$d_p = \frac{\rho g H'^2 k_s L}{4D'} \int_{\frac{x_0}{L}}^{\frac{x_0}{L}+1} p_m \frac{\partial p_m}{\partial z}\bigg|_{z=-1} dx = O\left(\frac{\rho g H'^2 k_s L}{4D'}\right) \tag{7}$$

According to the incident wave and bed conditions, the wave damping rate due to percolation, d_p, is in the order of 10^{-3} for the sandy bed and 10^{-8} for the silty bed. This shows that the percolation damping has insignificant effect on the wave damping for the experimental conditions investigated in this study.

Jonsson (1966) suggested that the bottom boundary layer (viscous damping) can be divided into laminar boundary layer and turbulent boundary layer by the critical wave Reynolds number, Re_{crit}, defined by

$$Re_{crit} = \frac{\pi^2}{32}\left(\frac{a_m}{\Delta}\right)^2 \tag{8}$$

where Δ is the Nikuradse roughness parameter. For a smooth bed, Δ equals to the

mean grain size and for a rough bed with ripples Δ equals to the height of the ripple (Jonsson, 1966). Flow in the boundary layer is turbulent, when the wave Reynolds number is larger than Re_{crit}. Based on equation (8), the boundary layer is laminar in tests No. 1, 2, 4 and 6, and is turbulent for tests No. 3 and 5 (see Table 3 for details). Liu and Orfila (2004) showed that the nonlinearity effect should be considered for the viscous damping in the laminar boundary layer. With considering the sidewall effect, their analytical solution for long progressive wave can be modified as

$$H' = H'_0 \exp\left(-\frac{1}{2\sqrt{2}} \frac{W'+h'}{W'} \sqrt{\frac{v_w}{h'\sqrt{gh'}}} \sqrt[4]{\frac{H'_0}{2h'}} \frac{x'}{h'} \right) \tag{9}$$

where W' is the half width of the wave flume. The comparison of the calculated normalized wave height by equation (9) (solid lines) with experimental measurements (close squares) is plotted in Figure 5. It is seen that the prediction by equation (9) agrees well with the measurements except in test No. 6 where the seabed is silt (note that the boundary layer in tests No. 3 and 5 is turbulent). It is seen that the predicted wave height is much larger than the measured data for test No. 6. Careful analysis of the experimental video shot for test No. 6 reveals that some soil particles are suspended near the bottom, as seen in Figure 6. This turbid layer will greatly increase the viscosity of water near the boundary layer due to the large viscosity of the silt and water mixture. This stimulates us to increase the viscosity in the boundary layer in equation (9). The predicted results using different viscosity are plotted in Figure 5 (*f*) which shows that the prediction agrees well with the experimental measurements when the viscosity is chosen as 7×10^{-5} m^2/s. This result is consistent with the field observations of Traykovshi et al. (2015).

For the turbulent boundary layer, the wave energy damping rate, d_f, induced by the bottom shear stress can be expressed by

$$d_f = \frac{1}{T}\int_0^T \tau_b u'_b dt \tag{10}$$

where τ_b is the shear stress at the bottom and is evaluated as (Jonsson, 1966; Nielsen, 1992):

$$\tau_b = \frac{1}{2}\rho f_w |u_b'| u_b', \qquad u_b' = u_{bm}' \cos(\omega' t') \tag{11}$$

Friction factor f_w can be determined by an empirical formula (Nielsen and Voulgaris 2014):

$$f_w = \begin{cases} \exp\left[5.213\left(\frac{a_m}{\Delta}\right)^{-0.194} - 5.977\right], & \frac{a_m}{\Delta} > 1.57 \\ 0.30, & \frac{a_m}{\Delta} \le 1.57 \end{cases} \tag{12}$$

Combining with equation (2), the wave energy damping rate can be further written as:

$$d_f = \frac{2\pi^2}{3}\rho f_w \frac{H'^3}{T'^3 \sinh^3 k'h'} \tag{13}$$

In addition, it is known that the wave energy is related to wave height. Based on the conservation law of wave energy flux, one has:

$$\frac{\partial c_g E}{\partial x} = -d_f \tag{14}$$

where c_g is the wave group velocity, E is the wave energy. Introducing the wave height damping rate, β_i, the wave height along the propagation direction can then be written as:

$$H' = H_0' e^{-\beta_i x'} \tag{15}$$

Combining equation (13), (14), (15) with the linear dispersion relationship yields the wave height damping rate:

$$\beta_i = \frac{4}{3\pi} \frac{k'^2 f_w H'}{\sinh k'h' \left(2k'h' + \sinh 2k'h'\right)} \tag{16}$$

The wave height calculated based on equations (15) and (16) is plotted in Figure 5 (*c*) and (*e*), respectively. The prediction using equation (9) for laminar boundary condition is also plotted in Figure 5 (*c*) and (*e*) for comparison. It is seen that the results calculated by equation (15) agree well with the measurements while large difference exists between the measurements and prediction by equation (9).

3.3. Wave damping in liquefaction tests

In the liquefaction tests, the surface soil layer behaves like fluid and oscillates with the wave although the displacement of the interface is much smaller than that of the free surface. Comparing with the non-liquefaction tests, wave damping over the liquefied seabed is more significant. For example, as shown in Figure 7, the eventual wave height measured by the wave gauge e in test No. 8 is as small as 3.39 cm, which is only 57.5% of the incident wave height. Based on linear wave theory, the energy dissipation is 66%. For test No. 9, the energy dissipation even reaches up to 77%, as the wave height damps over 50%. On the other hand, it can be found that the distribution of wave height varies with time. This is because the liquefaction front moves downward. Associated with the pore pressure records, it can be seen that the wave damping becomes significant, when the liquefaction depth increases from 2 cm to 27 cm, as indicated by the dash lines in the figure. This feature is seldom studied in previous experimental studies on wave-seabed interaction. For the sake of completeness, the normalized eventual wave height, H ($H = H'/H_0'$), measured by the gauges in the liquefied tests is plotted in Figure 8. By using exponential curve fitting method, the wave damping rate, β_i, can be determined to be -0.065 for test No. 7, -0.108 for test No. 8 and -0.171 for test No. 9.

These experimental results imply that the viscous dissipation in the mud layer becomes the primary damping factor when the silty is liquefied. To interpret this phenomenon, an analytical solution for wave motion over a viscous layer is presented in this study. Assume that the liquefied soil and water form a two-layered immiscible fluid system as shown in Figure 9. The upper water layer is treated to be inviscid as the water viscosity is much smaller than that of the liquefied soil. The liquefied soil layer is assumed to be uniform and viscous with a depth of d'. The water motion can be described by small amplitude wave theory and the liquefied mud motion is governed by Navier-Stokes equations. In addition, d' is in the same order of magnitude of the wave amplitude a' and the thickness of the Stokes boundary layer

for the liquefied mud, namely $O(k'a') = O(k'd') = O(k'\delta_m') = \lambda$. By using multiple-scale perturbation method, the wave damping rate can be solved as

$$\beta_i = r\frac{\delta_m' k_0^2}{2k_0 h + \sinh 2k_0 h}\frac{\sinh \hat{d}\cosh \hat{d} - \sin \hat{d}\cos \hat{d}}{\cos^2 \hat{d}\cosh^2 \hat{d} + \sinh^2 \hat{d}\sin^2 \hat{d}} \tag{17}$$

where h ($h = h'\omega'^2/g$) is the dimensionless water depth; r is the density ratio of the water to the liquefied mud, which equals to 0.59 in this study; $\hat{d}$ is the ratio of the thickness of the liquefied layer over that of the Stokes boundary layer; and k_0 is the leading order wavenumber which satisfies:

$$k_0 \tanh k_0 h = 1 \tag{18}$$

The detailed derivation process is presented in Appendix A. According to equation (17), the wave damping rate is increased when the liquefaction depth ranges from 0 to $1.5\delta_m'$, which agrees with Ng (2000).

Wave-induced residual liquefaction is a progressive process, which starts from the water-seabed interface and then moves downward (Sassa et al. 2001). In the experiments, the ranges of the liquefaction depth have been determined by the adjacent pore pressure transducers. For example, if the location of d'=2 cm is liquefied and the location of d'=9 cm is not liquefied, the liquefaction front will take place between the two adjacent pore pressure transducers at d'=2 cm and d'=9 cm. Above discussion shows that the eventual liquefaction depth is between 9 cm and 27 cm for the test No. 8 and between 27 cm and 40 cm for the test No. 9. To study the eventual viscous damping in the liquefied layer using the analytical solution, the damping rate with liquefaction depth of 2 cm, 9 cm, 27 cm and 40 cm is calculated by using equations (15) and (17). The calculated wave heights for tests No. 8 and 9 are plotted in Figure 8 as examples. Combining with the measurements of wave height, the analytical solutions show that the liquefaction front locates between 9 cm and 27 cm for the test No. 8. For test No. 9, the measurements and the analytical solutions

indicate that the thickness of liquefied layer is in the range of 27 cm to 40 cm. These results agree well with the pore pressure measurements, which implies that the viscous dissipation in the liquefied layer is the primary factor for wave damping. In Figure 8, the analytical solutions based on LC (2007) and Ng (2000) are also plotted for comparison. The results show that Ng's solution is very close to the present solution, while LC's solution is larger than the present solution. For test No. 8, these analytical results all agree with the measurements, but for test No. 9, LC's result is beyond the measured wave height range. The small difference between the present solution and Ng's solution is because the viscous effect in the water boundary layer is ignored in this study. Although water viscosity is increased in the silty bed tests due to the soil particles suspension, the viscosity of the liquefied mud is still much larger than that of the water. Therefore, the contribution due to the viscous damping in water boundary layer is small and weakened with the increase of the liquefaction depth. The relatively large error between LC and the present solution is mainly caused by the long wave assumption made in theoretical analysis of LC. Based on the long wave assumption, the Boussinesq approximation is employed in LC's study, namely $O(\epsilon)=O(\mu^2)$ (ϵ is the nonlinearity parameter and μ is the frequency dispersion parameter). However, in this study the waves belong to Stokes wave which is not sufficiently long to satisfy the Boussinesq approximation.

Analytical solution is also applied to explain the variation of the wave damping rate during the liquefaction process. As shown in Figure 3, the onset of liquefaction at locations of d'=2 cm, d'=9 cm and d'=27 cm is captured by the pore pressure transducers, associating with the liquefaction criterion. Meanwhile, the corresponding wave height distributions can be obtained using the time histories of the free surface elevation. The measurements show that the wave damping is not obvious in test No. 9, when the onset of liquefaction depth is located at $d' = 2$ cm. The wave height of the same phase over the liquefied region in test No. 9 with liquefaction depth of 9 cm and 27 cm can then be obtained and plotted in Figure 10 in which the lines are the

theoretical solutions calculated by equation (17), LC (2007) and Ng (2000), respectively. It is seen that all the calculated wave height distributions agree well with the measurements when the liquefaction depth is 9 cm. However, LC's solution is larger than the measured wave height when the liquefaction depth increases to 27 cm. Figure 10 indicates that the liquefaction depth increases with time, which in turn increases the wave height damping. It demonstrates that the viscous damping in the liquefied layer is the primary damping factor for silty seabed. This result concludes that soil liquefaction should be considered in the study of wave motion over silty seabed.

4. Conclusion

Laboratory experiments have been conducted to investigate the wave damping over sandy and silty bed. Water surface elevations and excess pore pressures are measured simultaneously during the experiments. The wave damping mechanism is analyzed associated with the wave induced seabed dynamic response. Analysis of experimental results indicates that the wave damping highly depends on the incident wave conditions and the property of bed medium. For the sandy beds, wave damping is limited to 7% and the primary damping mechanism is the bottom friction. Under certain conditions, sand ripples can be generated in the turbulent boundary layer, which can enhance the wave damping. For the silty beds, soil liquefaction can take place due to the wave loading. When the silty bed is liquefied, the wave height attenuation can reach up to 77% of the incident wave height. The analysis and observation show that the wave damping increases with the increase of the liquefaction depth. In this situation, the viscous flow in the liquefied layer is the primary damping factor.

Analytical analysis has been carried out to better understand and interpret the role of the viscous dissipation in the wave damping when seabed liquefaction takes place. The prediction using the analytical solution confirms the experimental finding that

when the seabed is liquefied, the wave height (thus the wave energy) is mainly damped by the viscous flow in the liquefied layer.

Notation

a'	wave amplitude
β_i	damping rate of wave height
β_r	shift of wave phase
C_g	wave group velocity
d'	liquefaction depth
$\tilde{d}$	ratio of the thickness of liquefied layer over that of Stokes boundary layer
d_p	energy dissipation rate due to percolation
d_f	energy dissipation rate due to viscosity
D'	thickness of the seabed
δ'_m	thickness of the Stokes boundary layer for the liquefied soil
δ'_w	thickness of the Stokes boundary layer for water
Δ	Nikuradse roughness parameter
e	void ratio of the soil
$e_{\max}$	maximum void ratio of the grain
$e_{\min}$	minimum void ratio of the grain
ξ'	displacement of the water-mud interface
E	wave energy
f_w	friction factor
g	acceleration of gravity
G	soil shear modulus
h'	water depth
H'	wave height
H'_0	incident wave height
η'	free surface elevation
k'	wave number
k_0	wavenumber at leading order
k_1	wavenumber at the first order
k_s	permeability coefficient of the soil
κ	local dimensionless coordinate in vertical direction
K_w	bulk modulus of elasticity of pure water
L	wavelength
λ	characteristic wave steepness
p'_m	wave-induced pore pressure in total
$\overline{p}$	wave-induced residual pore pressure
$\tilde{p}$	wave-induced oscillatory pore pressure

478	p_{max}	amplitude of wave-induced oscillatory pore pressure
479	p_b'	amplitude of the dynamic water pressure at the water-seabed interface
480	ϕ	velocity potential
481	r	density ratio of the water to the liquefied mud
482	Re	wave Reynolds number
483	ρ	density of water
484	ρ_m	density of liquefied mud
485	S_r	saturation degree of the sandy seabed
486	σ_{v0}'	initial vertical effective stress
487	τ_b	shear stress at the bottom of water column
488	u_{bm}'	amplitude of free stream velocity
489	v	Poisson's ratio
490	ν_m	viscosity of the liquefied layer
491	ν_w	viscosity of pure water
492	ω'	wave frequency
493	x'	coordinate in horizontal direction
494	$\chi^{(0)}$	variable χ at leading order
495	$\chi^{(1)}$	variable χ at first order
496	z'	coordinate in vertical direction

497

498 **Acknowledgement**

499 The authors are grateful for the support from the National Science Fund for
500 Distinguished Young Scholars (Grant No. 51425901), the National Key Research and
501 Development Program of China (2017YFC1404200), the Marine Renewable Energy
502 Research Project of State Oceanic Administration (GHME2015GC01), and the 111
503 Project (Grant No. B12032). The help and advice from Dr. Y. S. Park during the visit
504 of Dundee University are appreciated by the first author. Comments made by
505 reviewers greatly improved the quality of the final paper.

506

507 **Appendix A. Viscous damping over a liquefied layer**

508 As shown in Figure 9, we consider a wave train moving over a liquefied mud layer.
509 The dimensionless variables are introduced as follows:

510 For the liquefied mud

$$x = \omega'^2 x'/g, \quad \kappa = \left(z' + h' + d'\right)/d', \quad t = \omega' t', \quad \xi = \xi'/\lambda a' \tag{A1}$$

$$u_m = u_m'/\omega' a', \quad w_m = w_m'/\lambda\omega' d', \quad p_m = p_m'/\rho g a' \tag{A2}$$

where ξ' is the displacement of the water-mud interface, κ is a local dimensionless coordinate in vertical direction, p_m' is the dynamic pressure in the liquefied layer.

For water

$$\left(x,z\right) = \left(x',z'\right)\omega'^2/g, \qquad k = k' g/\omega'^2, \qquad \eta = \eta'/a' \tag{A3}$$

$$u = u'/\omega' a', \quad w = w'/\omega' a', \quad p = p'/\rho g a' \tag{A4}$$

where η' are the displacement of the free surface; p' are the dynamic pressure in the liquefied layer. Primes are used to distinguish the dimensional variables from their dimensionless counterparts. ξ' is considered one order smaller than η' (Macpherson, 1980; Ng and Zhang 2007). The governing equations for the liquefied layer and the water layer can then be written as following:

For the sub-liquefied soil layer, the dimensionless mass and momentum conservation equations can be expressed as:

$$\frac{\partial u_m}{\partial x} + \frac{\partial w_m}{\partial \kappa} = 0 \tag{A5}$$

$$\frac{\partial u_m}{\partial t} + \lambda u_m \frac{\partial u_m}{\partial x} + \lambda w_m \frac{\partial u_m}{\partial \kappa} = -r\frac{\partial p_m}{\partial x} + \frac{1}{d\,Re_m}\frac{\partial u_m}{\partial \kappa} + O\left(\lambda^2\right) \tag{A6}$$

$$-r\frac{\partial p_m}{\partial \kappa} + O\left(\lambda^2\right) = 0 \tag{A7}$$

where d equals to d'/a'; Re_m indicates the characteristic Reynolds number defined as:

$$Re_m = \frac{a'\omega' d'}{\nu_m} \tag{A8}$$

For silty seabed, ν_m is the order of magnitude of 0.01~0.1 m^2/s. We assume that $a' \sim 1\,\mathrm{m}$, $\omega' \sim 1\,\mathrm{Hz}$ and $d' \sim 1\,\mathrm{m}$, then Re_m is in the order of magnitude of 10~100 so that the liquefied layer shall be treated as viscous boundary layer. For the upper water layer, the dimensionless Euler equations can be written in the form of the velocity potential as following:

$$\frac{\partial^2 \phi}{\partial x^2} + \frac{\partial^2 \phi}{\partial z^2} = 0 \tag{A9}$$

$$p = -\frac{\partial \phi}{\partial t} - \frac{\lambda}{2}\left[\left(\frac{\partial \phi}{\partial x}\right)^2 + \left(\frac{\partial \phi}{\partial z}\right)^2\right] \tag{A10}$$

where ϕ is the dimensionless velocity potential.

To seek a solution of the two-layered fluid system, no-slip boundary condition is imposed at the bottom of the liquefied soil layer, as the displacement of the non-liquefaction soil is very small. Along the water-mud interface $z=-h+\lambda^2\xi$, the kinematic condition requires

$$\frac{\partial \phi}{\partial z} = \lambda \frac{\partial \xi}{\partial t} + O(\lambda^2) \tag{A11}$$

On the other hand, the stress at the interface should be continuous, namely

$$2\lambda d \frac{\partial u_m}{\partial x} n_x + \frac{\partial u_m}{\partial \kappa} n_z = O\left(\lambda^2\right), \qquad \frac{\partial u_m}{\partial \kappa} n_x + 2\lambda d \frac{\partial w_m}{\partial \kappa} n_z = O\left(\lambda^2\right) \tag{A12}$$

where $\boldsymbol{n}=(n_x, n_z)$ is the unit normal vector defined by:

$$n_x = \lambda^2 d \frac{\partial \xi}{\partial x} \frac{1}{\sqrt{1+\lambda^4 d^2 \xi_x^2}} = O\left(\lambda^2\right), \qquad n_z = \frac{1}{\sqrt{1+\lambda^4 d^2 \xi_x^2}} = O(1) \tag{A13}$$

On the free surface, the atmospheric pressure on the free surface is assumed to be zero. The kinematic and dynamic boundary conditions require:

$$\frac{\partial^2 \phi}{\partial t^2} + \frac{\partial \phi}{\partial z} = 0 \tag{A14}$$

To solve the above boundary value problem, multiple-scale perturbation method is employed and the solving process is given by Mei (1989). The leading order analysis is similar to that for waves moving over a rigid bed so that the solution for the water layer can be expressed as:

$$\phi^{(0)} = -i\frac{a}{2}\frac{\cosh k_0\left(z+h\right)}{\cosh k_0 h} e^{i(k_0 x - t)} + \text{c.c.} \tag{A15}$$

$$p^{(0)} = -\frac{a}{2}\frac{\cosh k_0\left(z+h\right)}{\cosh k_0 h} e^{i(k_0 x - t)} + \text{c.c.} \tag{A16}$$

It should be noted that the amplitude, a, is thus undetermined and is a function of the

slowly time scale t_1 ($t_1 = \lambda t$) and the small horizontal scale x_1 ($x_1 = \lambda x$). Substituting the above equations into the dynamic and kinematic boundary conditions, we obtain the expression of the free surface and the dispersion relation:

$$\eta^{(0)} = \frac{1}{2} a e^{i(k_0 x - t)} + \text{c.c.} \tag{A17}$$

$$k_0 \tanh k_0 h = 1 \tag{A18}$$

On the other hand, the leading order solution for the liquefied layer can be written as:

$$u_m^{(0)} = \frac{r k_0 a}{2 \sinh k_0 h} \left(1 - \cosh \vartheta\kappa + \tanh \vartheta \sinh \vartheta\kappa\right) e^{i(k_0 x - t)} + \text{c.c.} \tag{A19}$$

$$w_m^{(0)} = -\frac{i r k_0 a}{2\vartheta \sinh k_0 h} \left[\vartheta\kappa - \sinh \vartheta\kappa + \tanh \vartheta \left(\cosh \vartheta\kappa - 1\right)\right] e^{i(k_0 x - t)} + \text{c.c.} \tag{A20}$$

$$p_m^{(0)} = \frac{a}{2 \cosh k_0 h} e^{i(k_0 x - t)} + \text{c.c.} \tag{A21}$$

where ϑ is a constant and given by:

$$\vartheta = (1 - i)\hat{d}, \qquad \hat{d} = d'/\delta_m' \tag{A22}$$

Combining (A19), (A20) and (A21) with the kinematic boundary condition for the water-mud interface yields:

$$\xi^{(0)} = \frac{r k_0 a}{2\vartheta \sinh k_0 h} \left(\vartheta - \tanh \vartheta\right) e^{i(k_0 x - t)} + \text{c.c.} \tag{A23}$$

Based on the leading order solutions, the first order solution for the water layer can be further solved to give

$$\phi^{(1)} = i k_1 a \sinh k_0 \left(z + h\right) \left(C_g \sinh k_0 h - \frac{k_0 \left(z + h\right)}{2 k_0 \cosh k_0 h} \right) e^{i(k_0 x - t)} + \text{c.c.} \tag{A24}$$

$$p_m^{(1)} = -k_1 a \left(\frac{k_0 \left(z + h\right) \sinh k_0 \left(z + h\right)}{2 k_0 \cosh k_0 h} + C_g \sinh k_0 h \sinh k_0 \left(z + h\right) \right) e^{i(k_0 x - t)} + \text{c.c.} \tag{A25}$$

where C_g is the group velocity of waves. In addition, By applying Green's theorem to $\phi^{(0)}$ and $\phi^{(1)}$, the evolution equation of the free-surface wave amplitude, *a*, can be written as

$$\frac{\partial a}{\partial t_1} + C_g \frac{\partial a}{\partial x_1} = ik_1 C_g a \tag{A26}$$

where k_1 is the wavenumber at the first order and given by:

$$k_1 = \frac{2k_0^2 rd}{2k_0 h + \sinh 2k_0 h} \frac{\tanh \vartheta - \vartheta}{\vartheta} \tag{A27}$$

For monochromatic waves, the solution for Eq. (A26) can be written as:

$$a = a_0 e^{i\beta x'} = a_0 e^{ik_1 x_1} \tag{A28}$$

where β is a complex coefficient and can be written as $\beta=\beta_r+i\beta_i$. Finally, the wave damping rate β_i and the shift of wave number β_r can be obtained:

$$\beta_i = \mathrm{Im}\left(a' k_1\right) = \frac{r\delta'_m k_0^2}{2k_0 h + \sinh 2k_0 h} \frac{\sinh d' \cosh d' - \sin d' \cos d'}{\cos^2 d' \cosh^2 d' + \sinh^2 d' \sin^2 d'} \tag{A29}$$

$$\beta_r = \mathrm{Re}\left(a' k_1\right) = -\frac{2rk_0^2 d'}{2k_0 h + \sinh 2k_0 h}\left(1 + \frac{1}{2d'} \frac{\sin d' \cos d' + \sinh d' \cosh d'}{\cos^2 d' \cosh^2 d' + \sinh^2 d' \sin^2 d'}\right) \tag{A30}$$

Equation (A29) and (A30) are the same as those in Ng (2000) if water viscosity is ignored (ν_w=0) and the same as those in Mei et al. (2010) if the shear modulus of the liquefied mud is negligible (G=0). The analytical solution is validated by comparing with the experimental results reported by Hsu et al. (2013) who investigated the wave propagation over a mud layer of 8.77 m long and 0.06 m thick in a wave flume. In their experiments, the bulk density of the mud was 1.31 times larger than that of pure water. The free surface elevation over the mud was measured using eight wave gauges. More details about the experiments can be found in Hsu et al. (2013). Figure 11 shows the theoretically calculated and measured wave height distributions for two cases. The good agreement between the calculations and measurements shown in Figure 11 indicates that the analytical model can be used to estimate the wave damping over the

598 seabed with reasonable accuracy.

599

600 **References**

601 Chan, I.C., Liu, P.L.-F., 2009. Responses of Bingham-plastic muddy seabed to a
602 surface solitary wave. Journal of Fluid Mechanics 618, 155-180.

603 Chang, S.C., Lin, J.G., Chien, L.K., Chiu, Y.F., 2007. An experimental study on
604 non-linear progressive wave-induced dynamic stresses in seabed. Ocean
605 Engineering 34(17), 2311-2329.

606 Dalrymple, R.A., Liu, P.L.-F., 1978. Waves over soft muds: a two-layer fluid model.
607 Journal of Physical Oceanography 8, 1121-1131.

608 Foda, M., Tzang, S.Y., 1994. Resonant fluidization of silty soil by water waves.
609 Journal of Geophysical Research 99(C10), 463-475.

610 Elgar, S., Raubenheimer, B., 2008. Wave dissipation by muddy seafloors. Geophysical
611 Research Letters 35, L07611.

612 Gade, H.G., 1958. Effects of a non-rigid, impermeable bottom on plane surface waves
613 in shallow water. Journal of Marine Research 16, 61-82.

614 Garnier, E.I., Huang, Z.H., Mei, C.C., 2013. Nonlinear long waves over a muddy
615 beach. Journal of Fluid Mechanics 718, 371-397.

616 Hsu, J.R.C., Jeng, D.S., 1994. Wave-induced soil response in an unsaturated
617 anisotropic seabed of finite thickness. International Journal for Numerical and
618 Analytical Methods in Geomechanics 18(11), 785-807.

619 Hsu, W. Y., Hwung, H. H., Hsu, T. J., Torres-Freyermuth, A., Yang, R. Y., 2013. An
620 experimental and numerical investigation on wave-mud interactions. Journal of
621 Geophysical Research: Oceans 118, 1-16.

622 Hsu T W., Lan Y J., Lin Y S., 2018. Extended wind wave model (WWM)
623 incorporating the effect of submerged porous media with high permeability.
624 Coastal Engineering, 140, 87-99.

625 Jonsson, I.G., 1966. Wave boundary layer and friction factors. Proceedings of the 10th

International Conference on Coastal Engineering, ASCE, Tokyo, Japan, 127-148.
Kamphuis, J.W., 1978. Attenuation of gravity waves by bottom friction. Coastal Engineering 2, 111-118.
Kirca, V.S.O., Sumer, B.M., Fredsøe, J., 2013. Residual Liquefaction of Seabed under Standing Waves. Journal of Waterway, Port, Coastal and Ocean Engineering 139(6), 489-501.
Le Roux, J.P., 2012. Wave friction factor rediscovered. Geo-Marine Letters 32, 29-37.
Lin, Z.B., Guo, Y.K., Jeng, D.-S., Liao, C., Rey, N., 2016. An integrated numerical model for wave–soil–pipeline interactions. Coastal Engineering, 108: 25-35.
Lin, Z.B., Pokrajac, D., Guo, Y.K., Jeng, D.S., Tang, T., Rey, N., Zheng, J.H., Zhang, J.S., 2017. Investigation of nonlinear wave-induced seabed response around mono-pile foundation. Coastal Engineering 121, 197-211.
Liu, P.L.-F., Chan, I.C., 2007. On long-wave propagation over a fluid-mud seabed. Journal of Fluid Mechanics 579, 467-480.
Liu, P.L.-F., Orfila, A., 2004. Viscous effects on transient long-wave propagation. Journal of Fluid Mechanics 520, 83-92.
Liu, P.L.-F., Park, Y.S., L. Lara, J., 2007. Long-wave-induced flows in an unsaturated permeable seabed. Journal of Fluid Mechanics 586, 323-345.
Liu, P.L.-F., Simarro, G., Vandever, J., Orfila, A., 2006. Experimental and numerical investigation of viscous effects on solitary wave propagation in a wave tank. Coastal Engineering 53, 181-190.
Macpherson, H., 1980. The attenuation of water waves over a non-rigid bed. Journal of Fluid Mechanics 97, 721-742.
Mei, C.C., 1989. The applied dynamics of ocean surface waves. World Scientific Publishing, Singapore.
Mei, C.C., Krotov, M., Huang, Z.H., Huhe, A., 2010. Short and long waves over a muddy seabed. Journal of Fluid Mechanics 643, 33-58.
Mei, C.C., Liu, K.F., 1987. A Bingham-plastic model for a muddy seabed under long

waves. Journal of Geophysical Research 92(C13-14), 581-594.

Ng, C.O., 2000. Water waves over a muddy bed: a two-layer stokes' boundary layer model. Coastal Engineering 40, 221-242.

Ng, C.O., Zhang, X.Y., 2007. Mass transport in water waves over a thin layer of soft viscoelastic mud. Journal of Fluid Mechanics 573, 105-130.

Nielsen, P., 1992. Coastal bottom boundary layers and sediment transport. World Scientific Publishing, Singapore.

Nielsen, T.R., Voulgaris, G., 2014. Temporal and spatial evolution of wave-induced ripples geometry: Regular versus irregular ripples. Journal of Geophysical Research: Oceans 119, 664-688.

Okusa, S., 1985. Measurements of wave-induced pore pressure in submarine sediments under various marine conditions. Marine Geotechnology 6, 119-144.

Packwood, A.R., Peregrine, D.H., 1980. The propagation of solitary waves and bores over a porous bed. Coastal Engineering 3, 221-242.

Park, Y.S., Liu, P.L.-F., J. Clark, S., 2008. Viscous flows in a muddy seabed induced by a solitary wave. Journal of Fluid Mechanics 598, 383-392.

Putnam, J.A., Johnson, J.W., 1949. The dissipation of wave energy by bottom friction. Transactions, American Geophysical Union 30(1), 67-74.

Putnam, J.A., 1949. Loss of wave energy due to percolation in a permeable bottom. Transactions, American Geophysical Union 38(5), 662-666.

Qi, W.G., Gao, F.P., 2014. Physical modelling of local scour development around a large-diameter monopole in combined waves and current. Coastal Engineering 83, 72-81.

Reid, R.O., Kajiura, K., 1957. On the damping of gravity waves over a permeable sea bed. Transactions, American Geophysical Union 30(3), 349-356.

Sassa, S., Sekiguchi, H., Miyamoto, J., 2001. Analysis of progressive liquefaction as a moving-boundary problem. Géotechnique 51(10), 847-857.

Sassa, S., Takayama, T., Mizutani, M., Ponyol, N.M., 2006, Field observations of the

build-up and dissipation of residual porewater pressures in seabed sands under the passage of stormwaves. Journal of Coastal Research, 39, 410-414.

Seed, H.B., Rahman, M.S., 1978. Wave-induced pore pressure in relation to ocean floor stability of cohesionless soils. Marine Geotechnology 3(2), 123-150.

Sui, T.T., Zhang, C., Guo, Y.K., Zheng, J., Jeng, D.S., Zhang, J.S., and Zhang, W. 2016. Three-dimensional numerical model for wave-induced seabed response around mono-pile. Ships and Offshore Structures, 11(6), 667-678.

Sui, T.T., Zheng, J., Zhang, C., Jeng, D.S., Zhang, J., Guo, Y.K., He, R.. 2017. Consolidation of unsaturated seabed around an inserted pile foundation and its effects on the wave-induced momentary liquefaction. Ocean Engineering, 131: 308-321.

Sumer, B.M., Hatipoglu, F., Fredsøe, J., Sumer, S.K., 2006. The sequence of sediment behaviour during wave-induced liquefaction. Sedimentology 53, 611-629.

Sun, K., Zhang, J,S,, Gao, Y., Jeng, D.S., Guo, Y.K., Liang, Z.D., 2019. Laboratory experimental study of ocean waves propagating over a partially buried pipeline in a trench layer. Ocean Engineering 173: 617-627.

Tong, L.L., Zhang, J.S., Sun, K., Guo, Y.K., Jeng, D.S., 2018. Experimental study on soil response and wave attenuation in a silt bed. Ocean Engineering 160,105-118.

Traykovshi, P., Trowbridge, J., Kineke, G., 2015. Mechanisms of surface wave energy dissipation over a high-concentration sediment suspension. Journal of Geophysical Research: Oceans 120, 1638-1681.

Wen, J., Liu, P.L.-F., 1998. Effects of seafloor conditions on water wave damping. In: Tyvand, P.A. (Editor), Free-Surface Flows with Viscosity. Computational Mechanics Publications.

Yamamoto, T., Koning, H.L., Sellmeijer, H., Hijum, E.V., 1978. On the response of a pore-elastic bed to water waves. Journal of Fluid Mechanics 87(1), 193-206.

Zen, K., Yamazaki, H., 1990. Mechanism of wave-induced liquefaction and densification in seabed. Soils and Foundations 30(4), 90-104.

Zhang, C., Zhang, Q.Y., Zheng, J.H., Demirbilek, Z., 2017. Parameterization of nearshore wave front slope. Coastal Engineering, 127, 80-87.

Zhang, J.S., Jeng, D.S., Liu, P.L-F., 2011. Numerical study for waves propagating over a porous seabed around a submerged permeable breakwater: PORO-WSSI II model. Ocean Engineering 38(7), 954-966.

Zhang, J.S., Jeng, D.S., Liu, P.L-F., Zhang, C., 2012. Response of a porous seabed to water waves over permeable submerged breakwaters with Bragg reflection. Ocean Engineering 43(2), 1-12.

Zhang, J.S., Zhang, Y., Jeng, D.S., Liu, P.L.-F., Zhang, C., 2014. Numerical simulation of wave-current interaction using a RANS solver. Ocean Engineering 74, 157-164.

Zhao, H.Y., Jeng, D.S., Liao, C.C., Zhu, J.F., 2017. Three-dimensional modeling of wave-induced residual seabed response around a mono-pile foundation. Coastal Engineering 128, 1-21.

Zhu, G., Ren, B., Wen, H., Wang, Y., Wang, C., 2019. Analytical and experimental study of wave setup over permeable coral reef. Applied Ocean Research, 90, 101859 (doi：10.1016/j.apor.2019.101859)

Figure captions

Fig. 1. Experimental set-up (not to scale): (a) sandy bed; (b) silty bed.

Fig. 2. Vertical distribution of the normalized maximum excess pore pressure and analytical solutions by Hsu & Jeng (1994) (where D' is the thickness of the sediment basin and p_b' is the dynamic water pressure at the water-seabed interaction).

Fig. 3. Wave-induced pore pressure response along the vertical profile for the silty bed tests (where the red arrows indicate the onset of liquefaction, σ_{v0}' is the initial vertical effectives stress).

Fig. 4. Sand ripples observed in test No. 3.

738 Fig. 5. Comparison of the analytically predicted and measured wave damping for
739 non-liquefaction tests: (*a*) test No. 1; (b) test No. 2; (*c*) test No. 3; (*d*) test No. 4;
740 (*e*) test No. 5; (*f*) test No. 6.
741 Fig. 6. Time series of the video frames showing soil particles suspended near the
742 bottom in test No. 6.
743 Fig. 7. Time histories of the free surface elevation over the liquefied silty bed; the
744 dash green line indicates the onset of liquefaction for d' =2 cm, the red dash line
745 for d' =9 cm and the blue dash line for d' =27 cm.
746 Fig. 8. Distribution of the measured eventual wave height and the analytical results
747 over the sediment basin with analytical solution of Liu and Chan (2007) and Ng
748 (2000) for comparison: (*a*) test No. 8; (*b*) test No. 9.
749 Fig. 9. Definition for wave moving over a two-layered fluid system.
750 Fig. 10. Calculated and measured wave height distribution along the sediment basin
751 for test No. 9 with analytical solution of Liu and Chan (2007) and Ng (2000) for
752 comparison: (a) liquefaction front at d' =9 cm; (b) liquefaction front at d' =27
753 cm.
754 Fig. 11. Variation of wave height over the mud layer as observed in the experiment
755 and analytical results with incident wave height of 0.04 m, dynamic viscosity of
756 0.51 Ps·s for Case 2C and incident wave height of 0.08 m, dynamic viscosity of
757 0.65 for Case 4C (h' =0.24 m).
758
759 **Table captions**
760 Table 1. Physical properties of sediments used in the experiments.
761 Table 2. Summaries of the experimental conditions
762 Table 3. Friction factor and Nikuradse roughness parameter for the non-liquefaction
763 tests*
764
765
766

767 Fig. 1 tiff

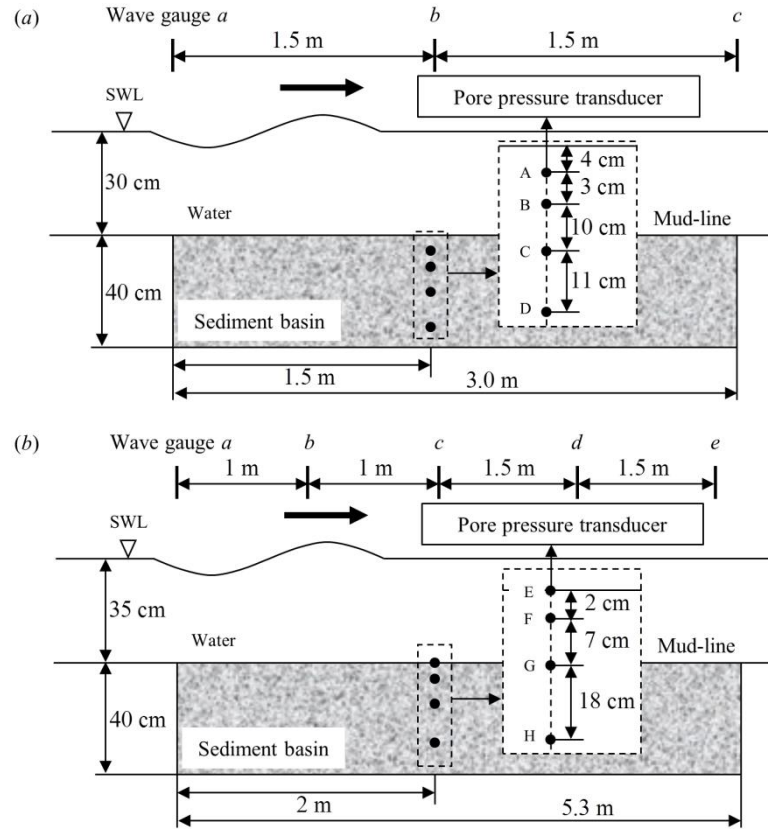

768
769

770 Fig. 2 tiff

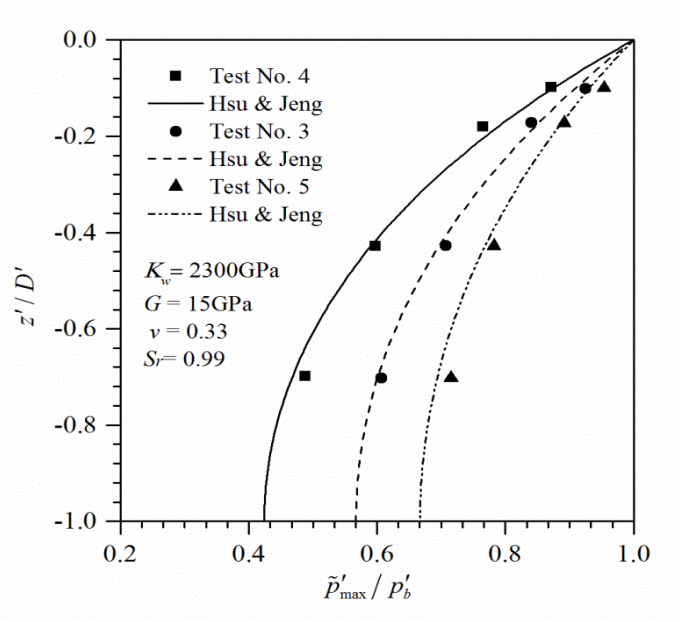

771

772

773 Fig. 3 tiff

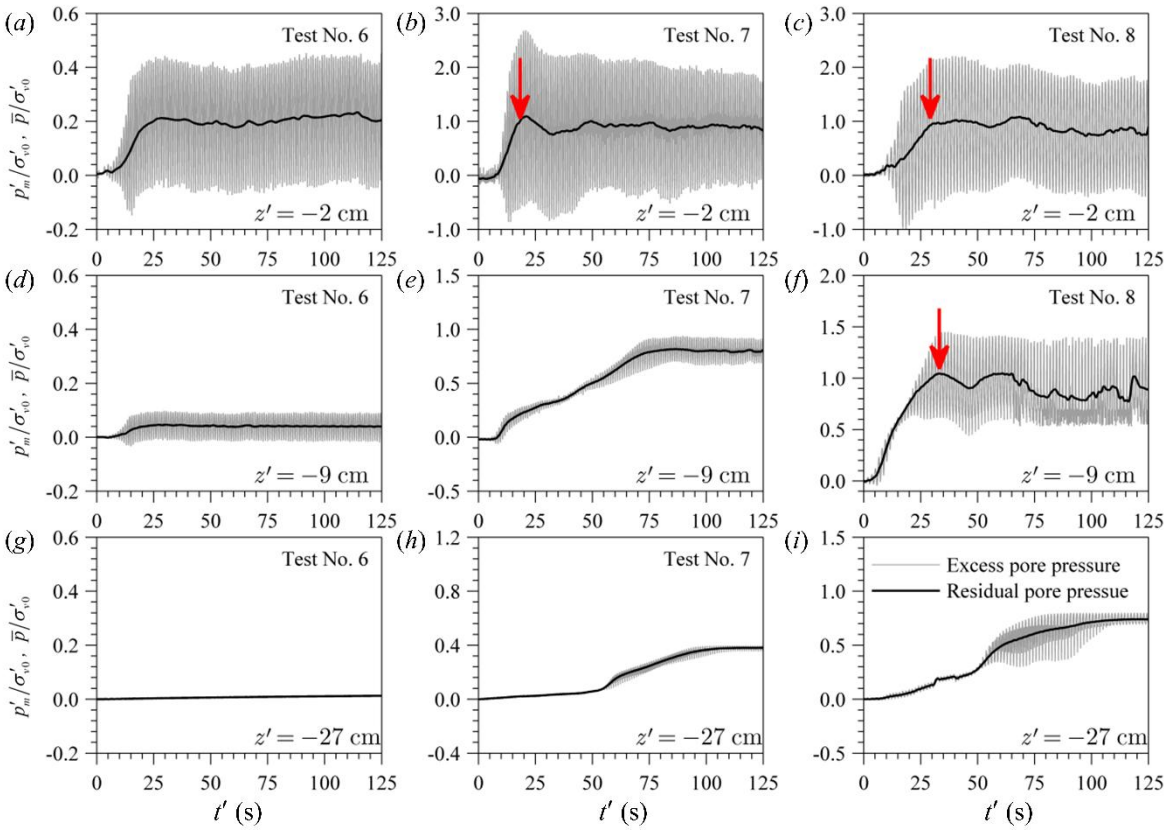

774

775

776 Fig. 4 tiff

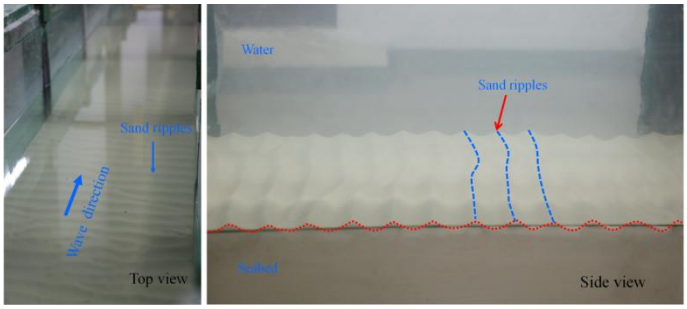

777
778

779 Fig. 5 tiff

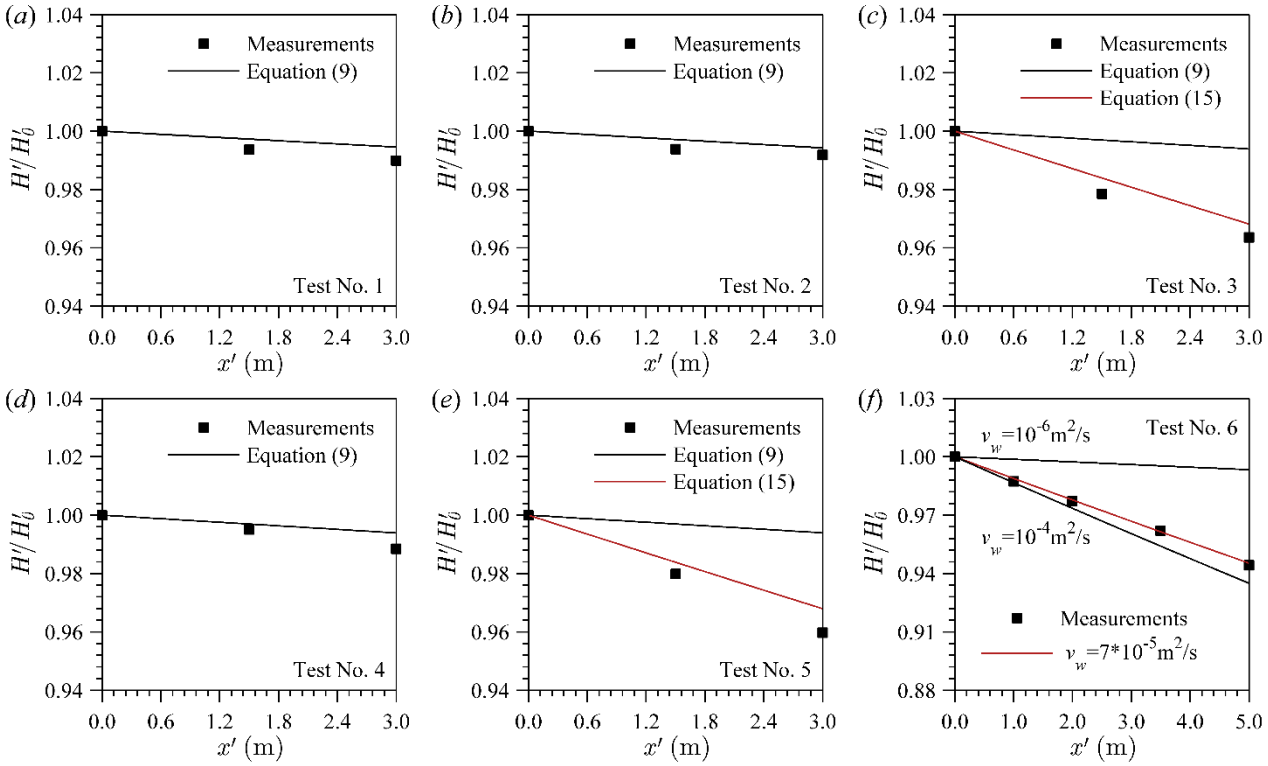

780
781

782 Fig. 6 tiff

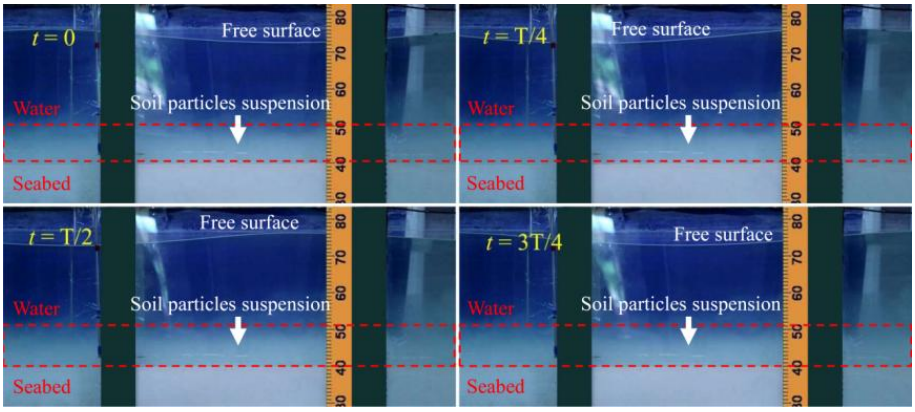

783

784

785 Fig. 7 tiff

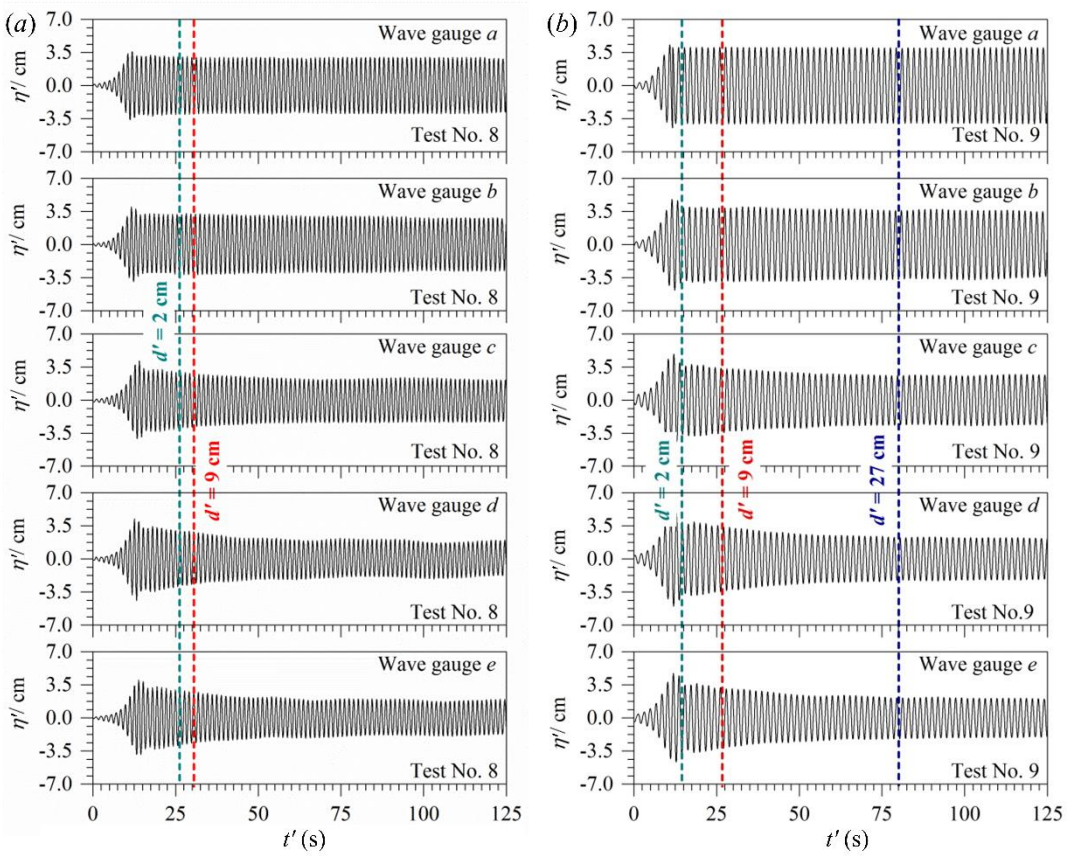

786
787

788 Fig. 8 tiff

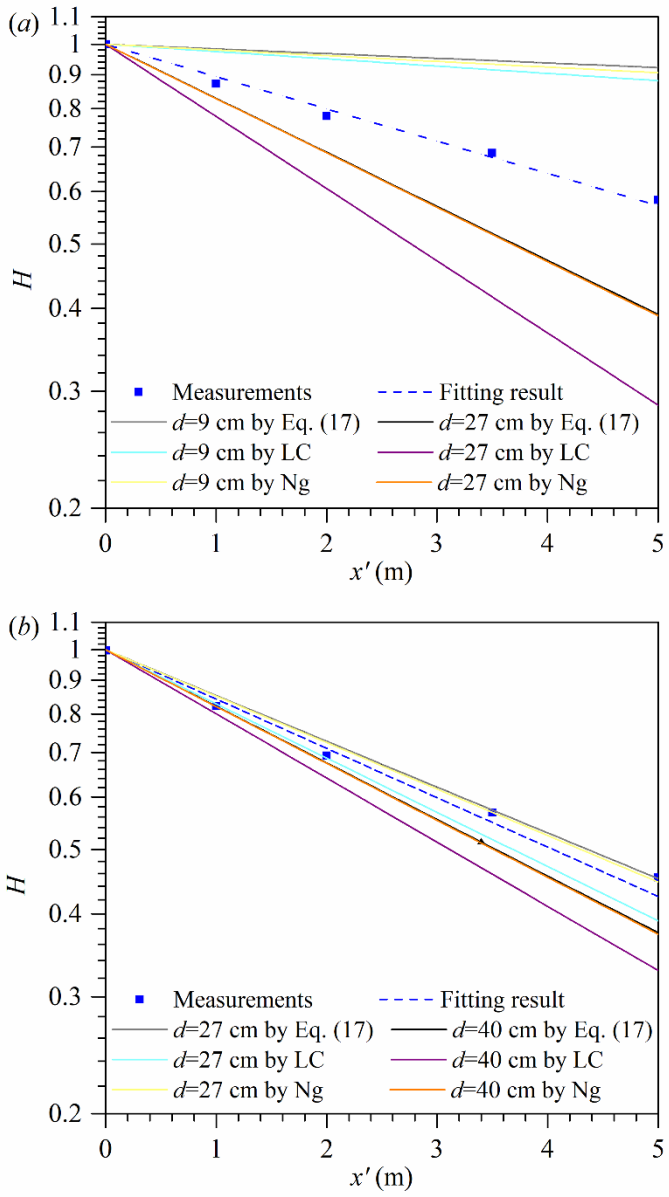

789
790

791 Fig. 9 tiff

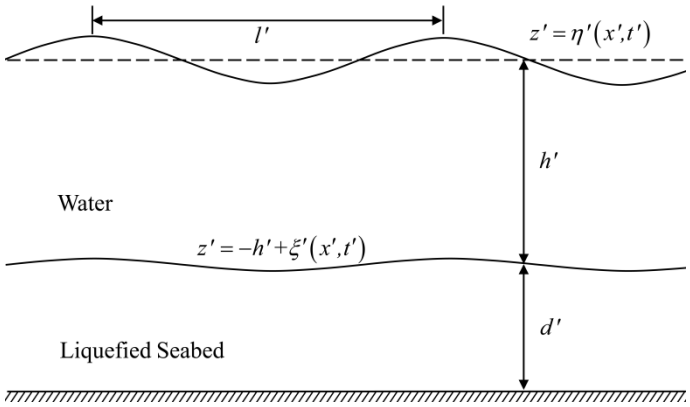

792

793

794 Fig. 10 tiff

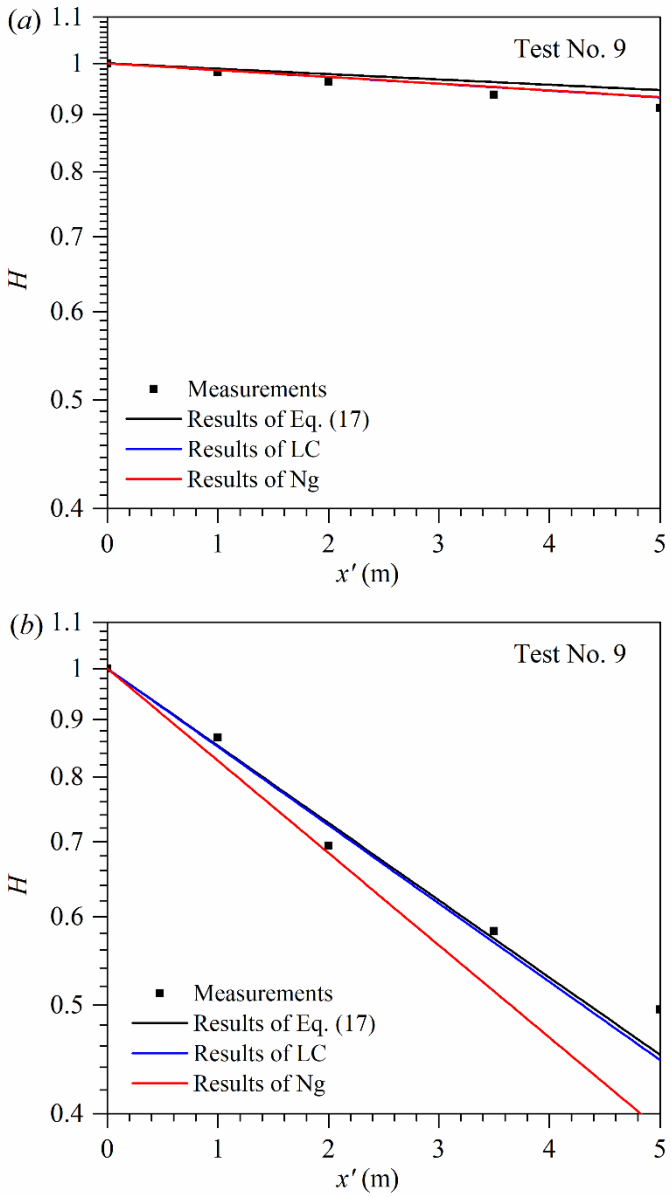

795

796

797

798 Fig.11 tiff

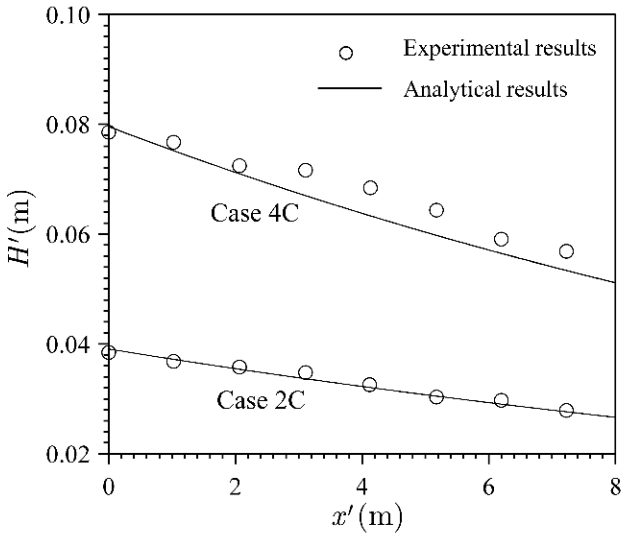

799
800
801
802
803
804
805
806
807
808
809
810
811
812
813
814
815
816
817
818

819

820

821